npj | quantum information

Article

Published in partnership with The University of New South Wales

https://doi.org/10.1038/s41534-024-00869-y

Coherence of a field gradient driven singlet-triplet qubit coupled to multielectron spin states in ^{28}Si/SiGe

Check for updates

Younguk Song [1,4], Jonginn Yun [1,4], Jehyun Kim[1], Wonjin Jang [1], Hyeongyu Jang[1], Jaemin Park[1], Min-Kyun Cho [1], Hanseo Sohn[1], Noritaka Usami[2], Satoru Miyamoto[2], Kohei M. Itoh [3] & Dohun Kim [1] ✉

Engineered spin-electric coupling enables spin qubits in semiconductor nanostructures to be manipulated efficiently and addressed individually. While synthetic spin-orbit coupling using a micromagnet is widely investigated for driving and entangling qubits based on single spins in silicon, the baseband control of encoded spin qubits with a micromagnet in isotopically purified silicon has been less well investigated. Here, we demonstrate fast singlet-triplet qubit oscillation (~100 MHz) in a gate-defined double quantum dot in ^{28}Si/SiGe with an on-chip micromagnet with which we show the oscillation quality factor of an encoded spin qubit exceeding 580. The coherence time $T_2{}^*$ is analyzed as a function of potential detuning and an external magnetic field. In weak magnetic fields, the coherence is limited by frequency-independent noise whose time scale is faster than the typical data acquisition time of ~100 ms, which limits the $T_2{}^*$ below 1 μs in the ergodic limit. We present evidence of sizable and coherent coupling of the qubit with the spin states of a nearby quantum dot, demonstrating that appropriate spin-electric coupling may enable a charge-based two-qubit gate in a (1,1) charge configuration.

Balancing the manipulation speed and coherence time, which often play opposing roles, has been a major goal of semiconductor quantum dot-based quantum information processing platforms[1–3] to maximize the qubit control fidelity. The electrical control of spin states is a representative example where, depending on the properties of the host material, either intrinsic[4,5] or extrinsic[6,7] spin-electric coupling methods have been explored. While strong spin-orbit coupling in compound semiconductors such as InAs and InSb enables fast Rabi oscillations[4,5], the fluctuations of the nuclear bath or susceptibility to charge noise due to strong spin-orbit coupling limit the inhomogeneous coherence time $T_2{}^*$ to the order of tens of nanoseconds. More recently, hole spins in group IV materials such as Ge (ref. 8) and Si (ref. 9) or electron spins in the Si-MOS structure[10] have been attracting much attention due to a more favorable ratio between the spin-orbit-based control speed and coherence time.

The electrons in silicon, in particular in the Si/SiGe heterostructure, have small intrinsic spin-orbit coupling[11]; therefore, an extrinsic method such as a micromagnet is necessary to rapidly manipulate its spin states. For single-spin qubits, the placement of an on-chip micromagnet has proven effective for both natural[7,12] and isotopically enriched silicon[13] in Si/SiGe and Si-MOS structures, where the field gradient provides fast control while not severely compromising the spin coherence. In the case of the silicon-based two-electron singlet-triplet qubit, however, the efficiency of the technique involving a micromagnet has not been fully examined. Previous studies of singlet-triplet qubit operation either used a small field gradient[14] or relied on the modulation of the exchange energy[15] in natural silicon. Exploration of the micromagnet technique with a field gradient in the intermediate range in isotopically purified silicon would thus be important for optimizing spin-electric coupling. In addition, this approach would enable this route to be compared with other methods such as the recently demonstrated spin-valley-driven coherent singlet-triplet oscillation in silicon[16,17].

Here, we demonstrate singlet-triplet qubit oscillation in a gate-defined double quantum dot in ^{28}Si/SiGe. An on-chip micromagnet is used to generate a magnetic field gradient that is sufficient to allow fast manipulation (oscillation frequency f_Q ~ 100 MHz), while benefiting from high spin coherence by isotopic enrichment. We measure the variation in the spin-electric coupling strength in the large valley-splitting regime (>175 μeV) in

[1]Department of Physics and Astronomy, and Institute of Applied Physics, Seoul National University, Seoul, Korea. [2]Graduate School of Engineering, Nagoya University, Nagoya, Japan. [3]Department of Applied Physics and Physico-Informatics, Keio University, Yokohama, Japan. [4]These authors contributed equally: Younguk Song, Jonginn Yun. ✉e-mail: dohunkim@snu.ac.kr

which an appropriate field gradient enables an encoded spin qubit to attain an oscillation quality factor over 580. We also present the analysis of the variation in T_2* as a function of experimental parameters such as detuning ε, magnetic field $B_{z,\mathrm{ext}}$, and gate tuning conditions, exploring the origin of the dominant noise source in the system. Moreover, we present evidence that the qubit engages in sizable and coherent coupling with the spin states of a nearby quantum dot, thereby demonstrating that the appropriate amount of spin-electric coupling may enable a different type of two-qubit gates of encoded spin qubits.

Results

The triple quantum dot system

Figure 1a shows a multiple quantum dot device fabricated on top of a ^{28}Si/SiGe heterostructure (see Methods for details of the material structure and device fabrication). We focus on a two-electron singlet-triplet (ST_0) qubit formed by the gate electrodes near the left Ohmic contact and a global top gate (not shown) while the regions beneath the other electrodes are fully accumulated. The general Hamiltonian H of the ST_0 qubit can be expressed as $H = J(\varepsilon)\sigma_z + \Delta B_z\sigma_x$, where $J(\varepsilon)$ is a ε-dependent exchange interaction with the Pauli matrix $\sigma_{i=x,y,z}$. ΔB_z is the magnetic field difference between the quantum dots constituting the qubit and is denoted in the frequency unit Hz using $\mathrm{T}g\mu_B/h$, where g, μ_B, and h are the Lande g-factor of the electrons in silicon, the Bohr magneton, and Planck's constant, respectively.

Additionally, we formed a third, many-electron quantum dot next to the ST_0 qubit to study the capacitive interaction between them. The design of the micromagnet on top of the device is similar to the ones used previously[18]. High frequency and synchronous voltage pulses, combined with the DC voltage through bias tees, were input to gates V_1, V_2, and V_T. Fast RF reflectometry[19,20] was performed by injecting a carrier signal with a frequency of approximately 125 MHz and power of −100 dBm at the Ohmic contact of the RF single-electron transistors on the left (see Fig. 1a). The reflected power was monitored through a chain of cryogenic and room temperature amplification and subsequent homodyne detection. The device was operated in a dilution refrigerator with a base temperature of approximately$\approx 7mK$, with $B_{z,\mathrm{ext}}$ ranging from −400 mT to 400 mT applied in the direction shown in Fig. 1a.

Figure 1b shows the charge stability diagram of the ST_0 qubit coupled with a many-electron quantum dot. The full specification of the number of electrons in the left, middle, and right quantum dots (QD_L, QD_M, QD_R, see green circles in Fig. 1a. For the position estimation sequence, see Supplementary Note 1) are denoted as (n,m,l), whereas the (n,m) notation is used whenever we focus on the ST_0 qubit only. A voltage pulse with a width of approximately 10 ns and rise time of 0.5 ns is input to V_1 and V_2 in the directions indicated by the red arrows in Fig. 1b. Near the charge transition from (0,2,N) to (1,1,N), the pulse abruptly changes the Hamiltonian to the form $H = \Delta B_z\sigma_x$, where the spin state initialized to the

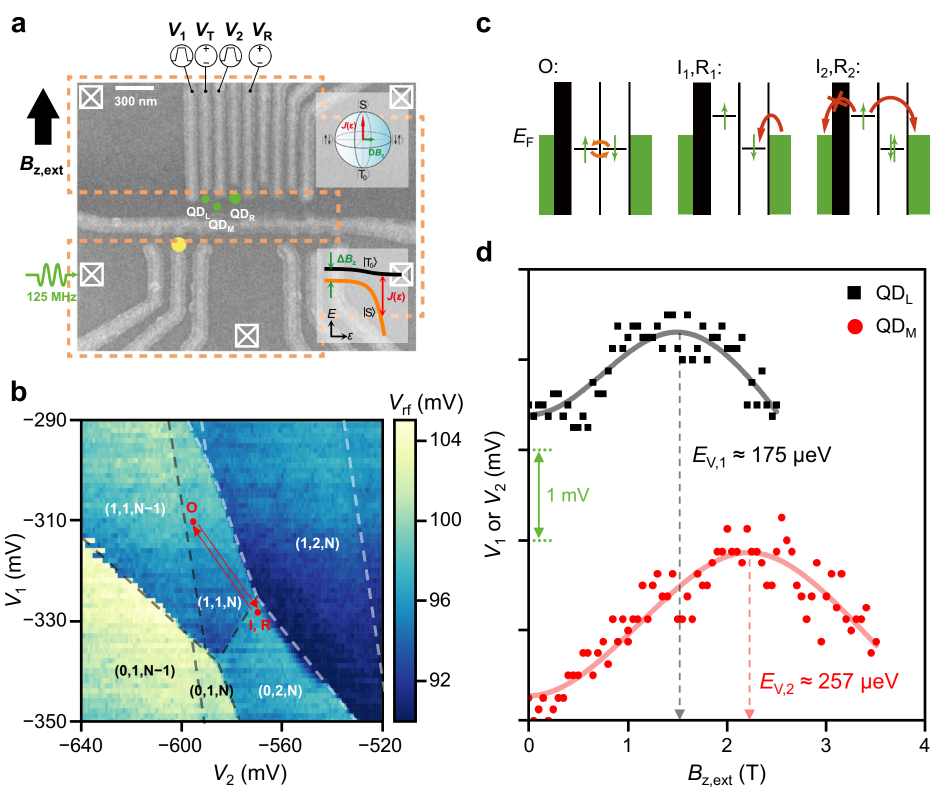

Fig. 1 | The quantum dot device and triple quantum dot system. **a** Scanning electron microscopy image of the device with the accumulation gates and Co micromagnet omitted. The black arrow indicates the direction of the external magnetic field $B_{z,\mathrm{ext}}$. We focused on three quantum dots, indicated by the green dots labeled QD_L, QD_M, and QD_R. We used QD_L and QD_M as the ST_0 qubit and the many-electron dot QD_R to explore the coherent interactions with the ST_0 qubit. High-frequency and synchronous voltage pulses combined with DC voltage were input to gates V_1, V_2, V_T, and V_R to tune and manipulate the quantum systems. The yellow dot indicates the sensor dot based on an RF single-electron transistor, with a transpassing RF signal of ~125 MHz through RF Ohmic contact (indicated by the crossed squares). The orange dashed line indicates the micromagnet employed to apply a magnetic field difference ΔB_z between QD_L and QD_M. The inset in the lower right corner illustrates the general energy level of the singlet and triplet states in a two-electron ST_0 qubit, with ΔB_z and detuning the ε-dependent exchange interaction $J(\varepsilon)$. The inset in the upper right corner depicts Bloch sphere representations of the contributions of $J(\varepsilon)$ and ΔB_z concerning the qubit rotation axis, with the two-electron states of the ST_0 qubit. **b** Charge stability diagram of the primary operational region for QD_L, QD_M, and QD_R. The number in parentheses represents the number of electrons in each of the three green dots. The inset shows V_{CDS}, the correlated double sampling signal of reflected RF signal V_{rf}. We drove the ST_0 qubit to reach I-O-R sequentially by applying appropriate pulse sequences with V_1 and V_2, while additional stopover points can be added to obtain the desired final qubit state. **c** Schematic of free evolution of the ST_0 qubit in O and the initialize/readout sequence in the I/R points in (**b**), respectively. **d** Measurement of the valley splitting of QD_L and QD_M via magnetospectroscopy.

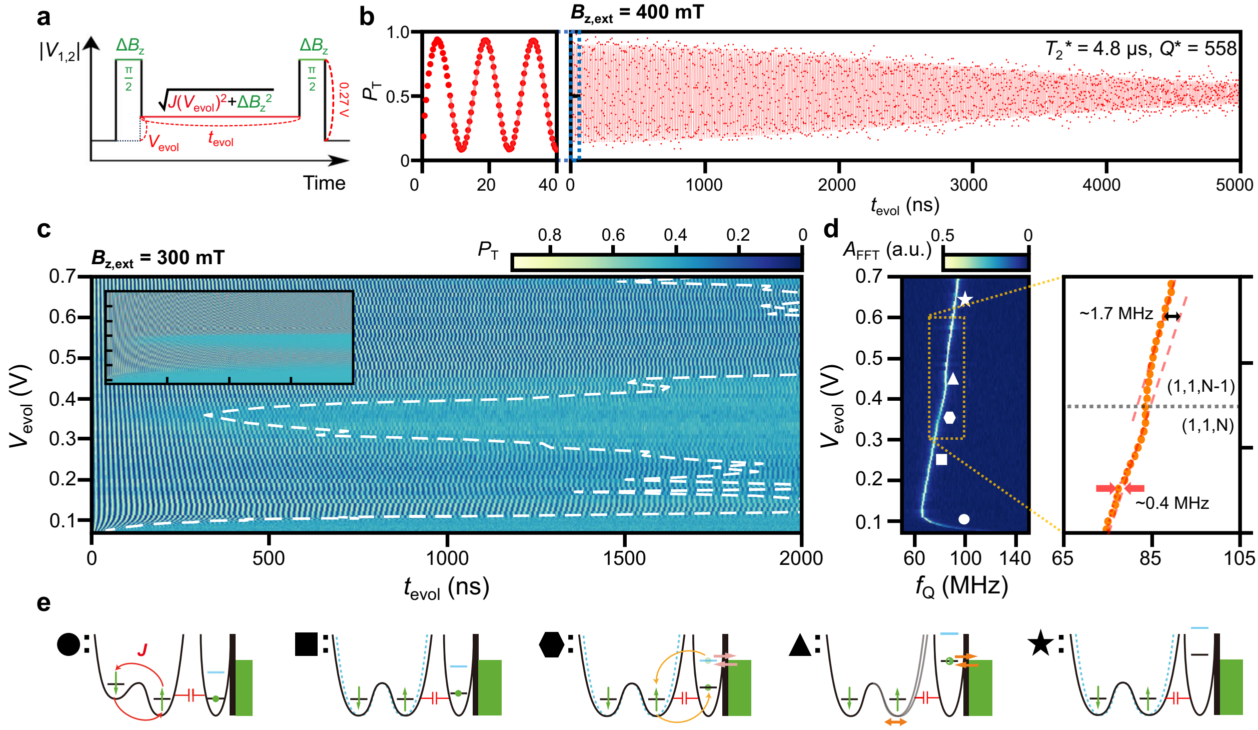

Fig. 2 | The qubit dynamics revealed by Ramsey interferometry. **a** Diagram of the pulse sequence used for Ramsey oscillation, the z-axis manipulation on the Bloch sphere with the free evolution time t_{evol}, and the pulse amplitude V_{evol}, with simultaneous control of $|V_1|$ and $|V_2|$. A π/2 pulse was applied with appropriately calibrated pulse duration time and V_{evol} = 0.27 V, where the ΔB_z contributes dominantly to the qubit rotation. **b** Representative Ramsey oscillation with the probability of the triplet state P_T at $B_{z,ext}$ = 400 mT and V_{evol} = 770 mV, with high coherence time T_2^* and quality factor Q^* values. The results on the left and right were averaged 10,000 and 100 times, respectively. **c** Ramsey oscillations as a function of t_{evol} and V_{evol}. The white dashed line indicates the contour line of T_2^* extracted from each Ramsey oscillation line of V_{evol}. The inset shows the numerically simulated Ramsey oscillation results. **d** Line-to-line fast Fourier transform (FFT) result of (**c**). The expected transition line of the dot on the right is indicated as a horizontal dotted line in the figure on the right. The two dashed orange lines show the linearly fitted f_Q with V_{evol} before and after the frequency shift of Δf_Q ~ 1.7 MHz during the charge transition of QD_R. A small bump with maximum Δf_Q ~ 0.4 MHz, indicated by the red arrows, is the footprint of the enhanced spin-dependent charge number fluctuation led by fast tunneling between QD_R and the electron reservoir on the right side of QD_R. **e** Schematic depicting the energy levels of each marker in (**d**), capacitive coupling between the ST_0 qubit and QD_R, and the tunneling between QD_R and the electron reservoir.

singlet rotates around the *x*-axis on the Bloch sphere (Larmor oscillations[11]), thereby resulting in a non-zero triplet state probability P_T. The discrimination of the resultant excited state population is conventionally performed by Pauli spin-blockade (PSB)-based spin-to-charge conversion[2,11,21] where the singlet and triplet spin states are mapped to the (0,2) and (1,1) charge configurations, respectively. However, ΔB_z produced by the micromagnet facilitates relaxation of the transient triplet (1,1) to the singlet (0,2) by mixing with the singlet (1,1) state, which makes a high-fidelity single-shot readout problematic[22].

To circumvent the problem, we adopted one of the latched-PSB techniques that maps the triplet state to a long-lived metastable charge configuration[23–25]. Pioneered in a similar experiment performed in a GaAs triplet quantum dot system[24], the version we used converts the triplet state (1,1) to the (1,2) state by rapidly loading an electron from the reservoir, which is expected to be located between QD_M, QD_R and the gate displayed as the horizontal gray line in Fig. 1a, at a tunneling rate greater than the sensor bandwidth of 10 MHz (Fig. 1c, middle panel). On the other hand, tunneling to the reservoir on the left is tuned to be of the order of 10 Hz. At this rate, the metastable (1,2) state can relax to a singlet (0,2) state only by indirect and slow tunneling of an electron from QD_L to the reservoir on the right (Fig. 1c, rightmost panel). Along with the higher signal contrast of a charge of one electron compared with conventional PSB, the prolonged relaxation time of the triplet states enables fast and high-fidelity single-shot measurement. The fast measurement capability is also important to examine the extent to which the variation in the qubit coherence time depends on the total data acquisition time to determine the effect of slow charge noise[26–28], as discussed in detail below.

Figure 1d shows the magnetospectroscopy measurements of the valley splitting[29] for QD_L and QD_M. By observing the crossover of the ground state from the singlet to the triplet by measuring the dependence of the energy required to add the second electron to each dot on $B_{z,ext}$, we obtain the valley splitting ~175 μeV (257 μeV) in QD_L (QD_M). The result confirms that the valley splitting in our device is at the largest energy scale of at least twice that of the Zeeman splitting at the maximum $B_{z,ext}$ applied in this study. Thus, we ignore the valley degree of freedom in this work and focus only on the ΔB_z-driven ST_0 qubit dynamics.

Qubit dynamics driven by the field gradient

With the calibrated π/2 pulse obtained from the Larmor oscillation measurement at the pulse amplitude $|\Delta V_1| = |\Delta V_2|$ = 270 mV, we construct a three-step pulse sequence for Ramsey interferometry (Fig. 2a). During the second step, at the pulse amplitude of free evolution $V_{evol} = |\Delta V_1| = |\Delta V_2|$, the qubit evolves around the axis of the Bloch sphere determined by the ratio of $J(V_{evol})$ and ΔB_z. Figure 2b shows a representative quantum oscillation at V_{evol} = 770 mV under the representative tuning conditions. This demonstrates a record-high[11,14,15] oscillation quality factor $Q^* = f_Q \times T_2^*$ = 116.25 MHz × 4.8 μs = 558 of a ΔB_z-driven ST_0 qubit rotation in the deep (1,1) charge configuration. Although the Q^* tends to decrease as $J(V_{evol})$ increases, the Q^* remains above 100 for $J(V_{evol})$ < 20 MHz, the regime where we expect that the high-fidelity two-axis control of ST_0 qubit can be implemented using AC driving[15]. In addition, high-resolution measurement (10,000 shots per data point with a single-shot readout time of 20 μs) of the first few oscillations (Fig. 2b, left panel) shows a readout visibility of ~85% (see Supplementary Note 2 for details on the signal-to-noise ratio).

To more fully understand spin-electric coupling and its effect on the coherence time, we mapped the dependence on the free evolution time t_{evol} and V_{evol} of the Ramsey interference at $B_{\mathrm{z,ext}} = 300$ mT, as shown in Fig. 2c. The oscillation observed for $V_{\mathrm{evol}} < 0.1$ V shows the fast but short-lived oscillation driven by J (marked as ● in Fig. 2d and the corresponding schematic diagram in Fig. 2e), whereas the oscillations driven by ΔB_z exhibit prolonged T_2* (white dashed contour in Fig. 2c) for $V_{\mathrm{evol}} > 0.1$ V due to the lower charge noise susceptibility $df_{\mathrm{Q}}/dV_{\mathrm{evol}}$. In this regime, the data in the time and frequency domains exhibit the following main features. First, f_{Q} is generally linearly dependent on V_{evol}, which arises from the presence of the micromagnet (see ▪ and ★ in Fig. 2d), and this is consistent with the previously observed linear shift of the single-spin resonance frequency in silicon in the presence of the synthetic field gradient[13]. Second, T_2* depends non-monotonically on V_{evol}. In particular, a significant decrease in T_2* is observed in the vicinity of $V_{\mathrm{evol}} = 0.35$ V (near ⬢ in Fig. 2d). Third, f_{Q} undergoes an abrupt frequency shift of about $\Delta f_{\mathrm{Q}} \sim 1.7$ MHz at approximately $V_{\mathrm{evol}} = 0.45$ V (▲ in Fig. 2d). Estimated from the calibrated lever arm of 0.023, the cross-talk effect of $V_{\mathrm{evol}} = 0.45$ V on $\mathrm{QD_R}$ shifts the chemical potential of $\mathrm{QD_R}$ to the Fermi-level of the right contact E_{F} where the ground state charge transition occurs. Therefore, the observed $\Delta f_{\mathrm{Q}} \sim 1.7$ MHz per one electron change is the measurement of the capacitive coupling between the $\mathrm{ST_0}$ qubit and $\mathrm{QD_R}$. We additionally verified this interpretation by adjusting the DC tuning of the plunger gate of $\mathrm{QD_R}$ and by observing the systematic shifts of the point ▲ (see Supplementary Note 3).

In general, the charge fluctuation in $\mathrm{QD_R}$ adversely affects the coherence of the capacitively coupled qubit. However, we note that $V_{\mathrm{evol}} = 0.35$ V (near ⬢ in Fig. 2d) showing the lowest T_2* occurs below $V_{\mathrm{evol}} = 0.45$ V (▲ in Fig. 2d) where $\mathrm{QD_R}$ experiences the maximum charge fluctuation. Assuming that non-negligible spin-dependent coupling occurs between the $\mathrm{ST_0}$ qubit and the Zeeman-split ground and excited spin states in $\mathrm{QD_R}$ occupied by N electrons (E_{g} and E_{e}, respectively), the qualitative interpretation of this phenomenon is as follows (See Supplementary Note 4 for data supporting spin-dependent coupling). For detuning near ■, the spin state in $\mathrm{QD_R}$ remains in the ground state with high fidelity as both E_{g} and E_{e} are well below E_{F}, and the spin-dependent charge fluctuation is low. From point ■ to ▲, as E_{e} approaches and passes E_{F}, fast tunneling between $\mathrm{QD_R}$ and the reservoir through E_{e} leads to enhanced spin-dependent charge number fluctuation. This fluctuation reduces T_2* and produces a small frequency shift of $\Delta f_{\mathrm{Q}} \sim 0.4$ MHz (red arrows in Fig. 2d). In this regime, the spin state in $\mathrm{QD_R}$ is expected to be a mixed state because of the non-negligible average occupation in E_{e}. The maximum charge fluctuation, hence the minimum T_2*, is expected to occur when E_{e} approximates E_{F}, which corresponds to the point ⬢. Finally, at point ▲, E_{g} aligns with E_{F}, resulting in the change in the full electron number in $\mathrm{QD_R}$ and the appearance of the kink in time-averaged f_{Q} measurement.

More quantitatively, we compared the experimental results with those of the numerical simulation[30] using the following phenomenological Hamiltonian and Lindblad operators, which were built based on the systematic analysis of Ramsey interferometry of the $\mathrm{ST_0}$ qubit discussed in the next section.

$$
\begin{aligned}
H = {} & J(V_{\mathrm{evol}})\sigma_{\mathrm{z}} \otimes \mathbf{1} + \Delta B_{\mathrm{z}}(V_{\mathrm{evol}})\sigma_{\mathrm{x}} \otimes \mathbf{1} \\
& + \beta(V_{\mathrm{evol}})\mathbf{1} \otimes \sigma_{\mathrm{z}} + \gamma(B_{\mathrm{z,ext}})\mathbf{1} \otimes \sigma_{\mathrm{x}} \\
& + J_{\mathrm{int}}(V_{\mathrm{evol}}) \tfrac{1}{e^{\eta(\beta(V_{\mathrm{evol}}-c))}+1} \sigma_{\mathrm{x}} \otimes \sigma_{\mathrm{z}} L_1 = \tau_1 \sqrt{J(V_{\mathrm{evol}})}\sigma_{\mathrm{z}} \otimes \mathbf{1}, L_2 \\
= {} & \tau_2 \sqrt{\beta(V_{\mathrm{evol}})}\mathbf{1} \otimes \sigma_{\mathrm{z}}
\end{aligned}
\tag{1}
$$

Here, the Hamiltonian describes the two interacting qubits, $\mathrm{ST_0}$ qubit, and the two spin states of the nearby N-electron quantum dot, $\mathrm{QD_R}$. More specifically, the Hamiltonian of the $\mathrm{ST_0}$ qubit is constructed as $J(V_{\mathrm{evol}})\sigma_{\mathrm{z}} + \Delta B_{\mathrm{z}}(V_{\mathrm{evol}})\sigma_{\mathrm{x}}$, where the background $\Delta B_{\mathrm{z}}(V_{\mathrm{evol}}) = 47.7\ V_{\mathrm{evol}} + 61.3$ ($0.25\ \mathrm{V} < V_{\mathrm{evol}} < 0.7$ V) is estimated from Fig. 2d. We assumed that the Hamiltonian of $\mathrm{QD_R}$ is analogous to that of the $\mathrm{ST_0}$ qubit, such that the diagonal term $\beta(V_{\mathrm{evol}})$ is an exponential function of V_{evol}, and the off-diagonal term $\gamma(B_{\mathrm{z,ext}})$ is a linear function of $B_{\mathrm{z,ext}}$. Furthermore, the coupling we consider is the spin-electric coupling induced from the spatial distribution of the orbital wavefunction of $\mathrm{QD_R}$ depending on its spin states. In view thereof, we chose the spin-electric coupled eigenstate of $\mathrm{QD_R}$ as the σ_z basis and introduced the interaction between the $\mathrm{ST_0}$ qubit and $\mathrm{QD_R}$, which was assumed to be in the form of $\sigma_x \otimes \sigma_z$. This coupling term is multiplied by a phenomenological Fermi−Dirac distribution with proper constant c, η and coupling strength $J_{\mathrm{int}}(V_{\mathrm{evol}})$ and to incorporate the change in the charge state of the nearby N-electron quantum dot (see Supplementary Note 5 for details of the simulation). Additionally, the phenomenological Lindblad operators for the $\mathrm{ST_0}$ qubit (L_1) and two-level system in $\mathrm{QD_R}$ (L_2) are introduced with the proportionality constant τ_1 (τ_2) to reflect the experimentally observed decoherence.

The inset in Fig. 2c shows the simulation result which consistently reproduces the sudden kink in the frequency near $V_{\mathrm{evol}} = 0.45$ V, the significant decrease in T_2* near $V_{\mathrm{evol}} = 0.35$ V, and the subsequent recovery of T_2* near the kink. Overall, by comparing the result of the simulation with that of the experiment, we concluded that the kink in the frequency and the drop in T_2* indicate capacitive coupling between the $\mathrm{ST_0}$ qubit and $\mathrm{QD_R}$ during the charge transition of $\mathrm{QD_R}$.

Coherent coupling between $\mathrm{ST_0}$ qubit and many-electron spin states

We further substantiated the validity of the above analysis by showing that the experimental and simulation results were consistently comparable under different quantum dot tuning conditions. Specifically, we fine-tuned the gate voltage levels to induce significant deviations in the overall coupling strength and the decoherence rates compared with the previous tuning condition. To establish the desired tuning condition, we primarily adjusted the gate V_{R} of Fig. 1a. In detail, while maintaining the optimal experimental parameters for qubit readout, we applied more negative voltage to the gate V_{R}, which is expected to increase J_{int} by decreasing the distance between $\mathrm{QD_M}$ and $\mathrm{QD_R}$. In this new tuning, we observed the characteristic beating of the quantum oscillation below $V_{\mathrm{evol}} < 0.42$ V, as shown in Fig. 3a. Notably, the coherence of the oscillation markedly diminished when the coupling between the two qubits became appreciable. Figure 3b enables a more detailed examination of these results and provides the line cuts that offer a clearer comparison between the oscillation traces in the uncoupled ($V_{\mathrm{evol}} = 0.6$ V, top trace in Fig. 3b) and coupled ($V_{\mathrm{evol}} = 0.2$ V, bottom trace in Fig. 3b) regimes.

The Ramsey interferometry of the $\mathrm{ST_0}$ qubit reveals the structure of the multielectron state in $\mathrm{QD_R}$. The observed beating oscillation of the $\mathrm{ST_0}$ qubit and the split of the corresponding FFT peak into two suggest that the multielectron state of $\mathrm{QD_R}$ is either a superposition or a mixed state of two different eigenstates. The interferometry of the $\mathrm{ST_0}$ qubit under different $B_{\mathrm{z,ext}}$ (see Supplementary Note 4 for the low $B_{\mathrm{z,ext}}$ result) shows that the degree of beating decreases and eventually disappears as $B_{\mathrm{z,ext}}$ decreases, revealing that the degree of mixing of the two $\mathrm{QD_R}$ states is inversely proportional to $B_{\mathrm{z,ext}}$. Furthermore, the dependence of the beating of the oscillation on V_{evol} suggests that the degree of mixing of the eigenstates of $\mathrm{QD_R}$, whose orbital wavefunction directly couples with f_{Q} through spin-electric coupling, is a function of V_{evol}. The significant drop in T_2* in the regime of sizeable coupling is again likely a consequence of the interplay between the interqubit coupling and the dephasing effect discussed in the previous section. Nonetheless, the interqubit coupling rate is faster than the decoherence rate, suggesting the possibility of entangling an $\mathrm{ST_0}$ qubit with the multielectron level in $\mathrm{QD_R}$. Additionally, the coupling strength with the maximum value of approximately 10 MHz also exhibits a dependence on V_{evol}, highlighting the electrical tunability of the interqubit coupling strength. The phenomenological Hamiltonian we introduced in the previous section summarizes these findings.

This experimental result was compared with the numerical simulation, which employed the identical Hamiltonian and Lindblad operators introduced in the previous section, whose parameters were appropriately

Fig. 3 | Coherent coupling between the singlet-triplet qubit and many-electron spin states. a Left: Ramsey oscillations as a function of t_{evol} and V_{evol} for different tuning levels. Significant dephasing appears below $V_{evol} = 0.42$ V. Right: FFT result of the figure on the left. The FFT peak exhibits the characteristic kink near $V_{evol} = 0.5$ V and linear dependence on V_{evol} in the ΔB_z-dominating regime. Characteristic splitting of the FFT peak is also manifested below $V_{evol} = 0.42$ V. **b** Ramsey oscillation trace at $V_{evol} = 0.6$ V (top, red squares) and 0.2 V (bottom, black solid circles). The beating of the oscillation at $V_{evol} = 0.2$ V is manifested. Each trace corresponds with the dashed line in the respective color in (**a**). The traces are offset by 1 for clarity. **c** Left: Numerical simulation of Ramsey oscillations as a function of t_{evol} and V_{evol}. The significant decoherence below $V_{evol} = 0.42$ V was reproduced consistently. Right: FFT result of the figure on the left. The FFT peak shows the kink near $V_{evol} = 0.5$ V, a V_{evol} dependence similar to the experimental results, and the characteristic splitting below $V_{evol} = 0.42$ V. **d** Simulated Ramsey oscillation trace at $V_{evol} = 0.6$ V (top, red squares) and 0.2 V (bottom, black solid circles). The simulated oscillation trace also reflects the beating of the oscillation at $V_{evol} = 0.2$ V. Each trace corresponds with the dashed line in the respective color in (**c**). The traces are offset by 1.2 for clarity.

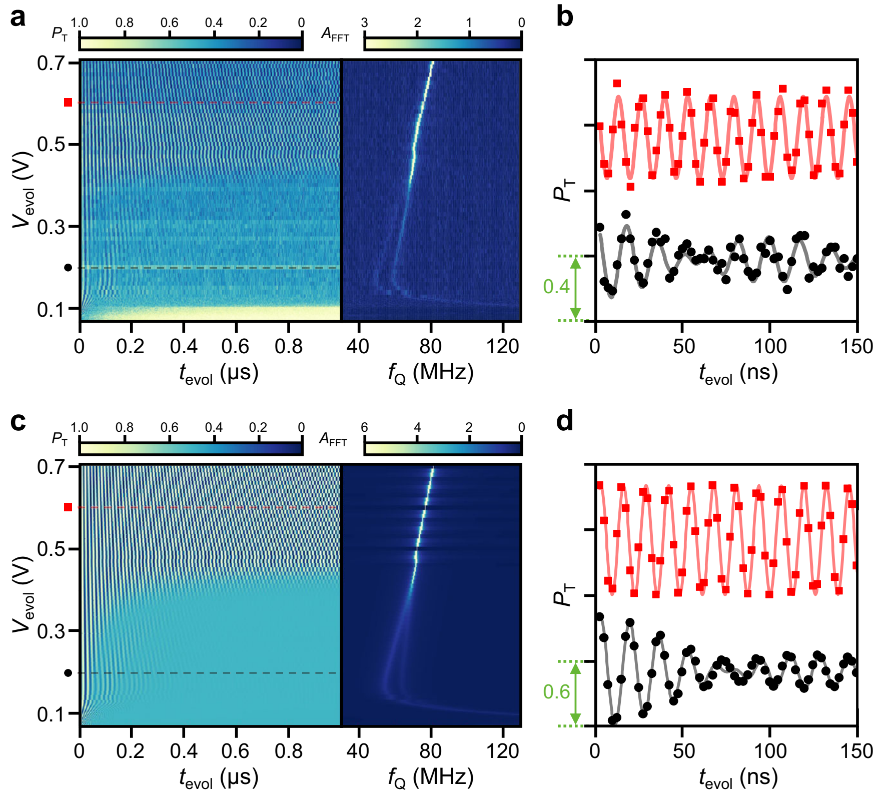

adjusted to reflect the different tuning conditions. One of the key adjustments involves the parameters of $\beta(V_{evol})$, which effectively transform the eigenstate of QD_R into the superposition of the σ_z-eigenstates for $V_{evol} < 0.4$ V, which gives rise to the observed beating of the oscillation through the spin-electric coupling $\sigma_x \otimes \sigma_z$ term. The numerical calculation consistently reproduces the experimental results, including the characteristic kink near $V_{evol} = 0.48$ V, the emergence of the beating, and the significant reduction in T_2^* throughout the coupling regime. These observations can be attributed to the mixed eigenstate of QD_R and the Lindblad operators, which effectively mimic the aforementioned dephasing effect. Overall, our spin-electric coupling scenario convincingly reproduces the experimental results for various coupling parameters.

External field dependence of ST_0 qubit coherence

We turn to discuss the dominant noise source limiting the coherence of ST_0 qubit by investigating the variation in f_Q and df_Q/dV_{evol} as a function of $B_{z,ext}$. The magnitude of the field gradient $|\Delta B_z|$ is determined by measuring f_Q of the ΔB_z-dominated Ramsey oscillations at $V_{evol} = 800$ mV for various values of $B_{z,ext}$ from 400 mT to −400 mT (Fig. 4a). Generally, $|\Delta B_z|$ was positively correlated with $B_{z,ext}$, which likely originated from the formation of multiple domains due to the demagnetization of the Co micromagnet at low $B_{z,ext}$. The calculated value expected for $|\Delta B_z|$ by simulation of the magnetic field using the Object Oriented Micromagnetic Framework (OOMMF)[31,32] was in qualitative agreement with the experimental observation. (see Supplementary Note 6 for details of the micromagnetic simulation).

The controllability of $|\Delta B_z|$ via $B_{z,ext}$ paved the way to test whether a decrease in $|\Delta B_z|$ could lead to a smaller df_Q/dV_{evol} and, consequently, an improved T_2^* at low $B_{z,ext}$. Figure 4b shows the dependence of df_Q/dV_{evol} on f_Q, extracted at various levels of $B_{z,ext}$ and V_{evol}. Unexpectedly, a strong correlation did not exist between f_Q and df_Q/dV_{evol}. Depending on the experimental iteration, df_Q/dV_{evol} was widely dispersed even at similar f_Q controlled by V_{evol}. We again attribute this to the nanoscale formation of

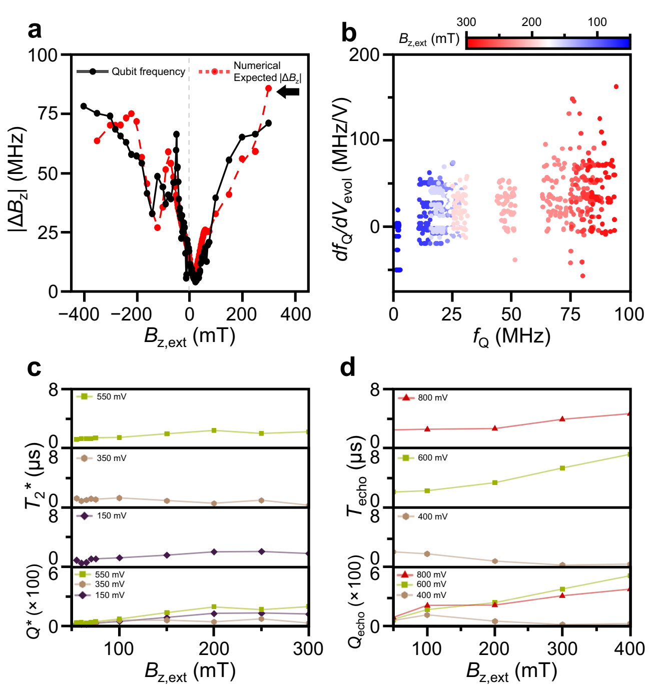

Fig. 4 | External magnetic field dependence of coherence time. a Estimated $|\Delta B_z|$ extracted from f_Q of the Ramsey oscillation performed for $V_{evol} = 800$ mV in the ΔB_z-dominating region (black), and expected $|\Delta B_z|$ from the magnetic field simulation using OOMMF (red) (see Supplementary Note 6). The black arrow indicates the direction of the measurement. **b** Extracted f_Q and charge susceptibility df_Q/dV_{evol} of the qubit in $B_{z,ext}$ of 300−40 mT and V_{evol} of 0.4−0.7 V. df_Q/dV_{evol} was derived with interpolated f_Q. **c** Measured T_2^*, Q^* of the Ramsey oscillations as a function of $B_{z,ext}$ at various V_{evol}. **d** T_{echo} and Q_{echo}, the results of the spin-echo experiment of $T_2^*$and Q^*, respectively, as a function of $B_{z,ext}$ at various V_{evol}.

multiple domains in the micromagnet, which generates a locally inhomogeneous field distribution.

Figure 4c shows T_2^* and Q^* as functions of $B_{z,ext}$ at several V_{evol}. Generally, the decreasing Q^* is predominantly the result of the rapid decrease in f_Q as the applied magnetic field $B_{z,ext}$ weakens, whereas T_2^* varies at most by a factor of two as a function of $B_{z,ext}$. The latter finding is also consistent with the observation that f_Q and df_Q/dV_{evol} are not strongly correlated. Although T_2^* tends to increase in the presence of strong $B_{z,ext}$, we argue that this is because of the interplay between the experimental data acquisition time and dominant noise band, which shifts to the low frequency at stronger $B_{z,ext}$. We confirm that extending the total data acquisition time significantly affects T_2^* at $B_{z,ext} = 400$ mT, indicating that slow charge noise compared to a given measurement time plays an important role (see Supplementary Note 7). Moreover, near $V_{evol} = 350$ mV, where T_2^* is limited by strong coupling with the spin states in QD_R and fast charge noise is therefore presumed to dominate the noise spectrum, T_2^* is nearly constant as a function of $B_{z,ext}$. In this respect, we assume that T_2^* at low $B_{z,ext}$, which approximates 1 µs regardless of the value of V_{evol}, is entirely dominated by the noise spectrum, which is faster than the measurement time. This indicates that the coherences of the ST_0 qubit are closer to the ergodic limit.

The dominance of high-frequency noise in our system is also supported by measurement of the spin-echo time T_{echo} and echoed quality factor Q_{echo} at various $B_{z,ext}$ and V_{evol} (Fig. 4d). Notably, the spin-echo enables only a minor improvement in the coherence time by a factor of at most two compared with T_2^* at low $B_{z,ext}$ of ~100 mT, thereby indicating that the major source of noise in this regime is in the high-frequency band. Similar ineffectiveness of the spin-echo was observed in a ^{Nat}Si/SiGe-based singlet-triplet qubit for non-negligible J (ref. 33). Although a previous study[34] pointed out that the increased flip-flop motion of residual ^{29}Si nuclear spins at low $B_{z,ext}$ leads to the reduction of T_2^*, we rule out this possibility since we expect that the nuclear spin flip-flop rate is suppressed below 10 Hz by the presence of on-chip micromagnet[35,36]. Moreover, this type of noise is more likely to occur under RF excitations needed for single-spin qubit manipulation. The absence of such control in this experiment also indicates that the mechanism of the dominant noise source at low $B_{z,ext}$ in our experiment differs from that in the previous study. The spin-echo more effectively enhances the coherence time at high $B_{z,ext} > 300$ mT, which is consistent with our scenario that, in this regime, the dominant noise primarily stems from the low-frequency band. Similar to the behavior of T_2^*, the spin-echo is not effective when the ST_0 qubit is strongly coupled with QD_R (see Fig. 4d, third panel).

We additionally compared the power spectral density (PSD) of noise for strong and weak magnetic fields, $B_{z,ext}$ (400 and 50 mT, respectively) obtained by the single-shot measurement-based rapid Bayesian estimation method[26,37,38] (see also Supplementary Note 8) as shown in Fig. 5a. Although both of these spectra exhibit a larger white noise component compared to previous studies[28,33], the PSD of the spectrum at $B_{z,ext} = 50$ mT is about two orders of magnitude larger across the entire range of frequencies with different exponent α of the $1/f^{\alpha}$-like power spectrum compared to the PSD at $B_{z,ext} = 400$ mT. Assuming that the frequency-independent noise extends to frequencies beyond the experimentally measured limit of ~40 Hz, the result explains the overall ineffective noise refocusing via the spin-echo technique in our system, in particular at low $B_{z,ext}$. In addition, the tendency of the white noise floor to increase with decreasing $B_{z,ext}$ along with the change in α (Fig. 5b), which is generally indicative of a relative increase in the portion of fast charge noise, is consistent with the variation in T_2^* and T_{echo}, as presented in Fig. 4.

Discussion

The origin of the rather high white noise floor in our system, which further increases at low $B_{z,ext}$, remains an open question. Although a more comprehensive understanding of the dominant noise source would require further experiments, the ineffective coherence recovery using the spin-echo technique due to relatively fast noise indicates that the noise does not predominantly originate from the increased flip-flop rate of the residual ^{29}Si nuclear spins. Based on our investigation of the signature of the nanoscale multi-domain structure as the micromagnet demagnetizes at $B_{z,ext} < 200$ mT, we speculate that the fast noise could have stemmed from the interplay between the field inhomogeneity induced by the magnetic domain structure and charge noise. This could be clarified by studying multiple devices containing micromagnets with various magnetic properties. A potential approach could involve the use of different techniques for micromagnet fabrication; for example, the deposition of magnetic material in the presence of an applied magnetic field, which is known to induce a preferential magnetization axis and hence a significantly modified hysteresis loop[39]. This technique may enable the magnetic structure to be more stably controlled in a weak magnetic field, which would allow an investigation of the transduced noise with varying magnetic properties. Moreover, the technique could also be useful for other applications such as semiconductor-superconductor hybrid circuits[40,41] for long-range coupling where operation in a weak magnetic field is beneficial.

Nevertheless, we successfully demonstrated coherent ST_0 oscillations with outstanding Q^*. This was enabled by using an on-chip micromagnet technique in an isotopically purified ^{28}Si/SiGe heterostructure where f_Q is tunable in the (1,1) charge configuration due to the dependence of the magnetization on $B_{z,ext}$. Our findings reveal that capacitive coupling can facilitate coherent interactions between two quantum systems: the two-electron ST_0 qubit and the many-electron quantum dot. Moreover, by formulating Hamiltonians for these quantum systems and their interactions, we effectively reproduced the coherent ST_0 qubit oscillation observed in our experiments through numerical simulation. Our work also suggests areas for improvement. Even though our device was designed to allow us to coarsely tune the chemical potential of QD_R, independent control of the quantum states of QD_R was challenging because of the limited number of control lines in the current single-gate layer structure. Enhanced control over individual quantum dots and precise coupling strength modulation

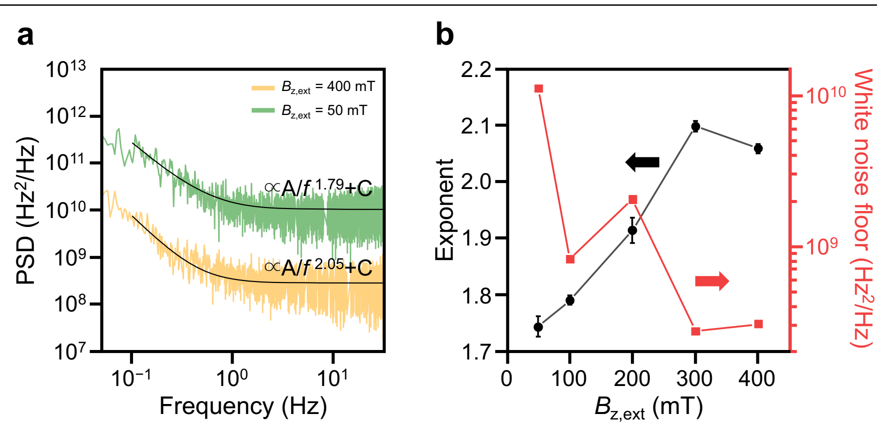

Fig. 5 | Noise spectrum analysis. a Noise spectrum acquired by applying two different $B_{z,ext}$. Power spectral densities (PSDs) were derived by analyzing single-shot data with the rapid Bayesian estimation method (see Supplementary Note 8). Each noise spectrum was calculated using 100,000 single shots. Offsets were excluded from this figure. **b** Power-law exponent and white noise floor level obtained from the noise spectrum at each $B_{z,ext}$.

could be attained by adopting an overlapped gate structure[42], which may enable different two-qubit gate schemes for encoded spin qubits in silicon.

Methods

Material structure and device fabrication

The ^{28}Si/SiGe heterostructure wafer was grown by a molecular beam epitaxy growth method. An isotopically purified silicon source (with a residual ^{29}Si concentration of approximately 800 ppm) was used for the strained quantum well with a thickness of 12 nm. The design of the surface gate electrode resembles that of GaAs spin qubit devices where both quantum dot confinement and barrier gates reside in the same layer and a global accumulation gate is used for electrostatic doping. The dimensions of the accumulation gate were maintained below $2 \times 2\,\mu m^2$ to minimize the parasitic capacitance[20], enabling proper impedance matching conditions for radio frequency (RF) reflectometry. A Co micromagnet was deposited above the accumulation gate using an e-beam evaporator, with a Au cap for the antioxidation layer.

Measurement setup

The sample was cooled to the base temperature, ~7 mK, with a cryogen-free dilution refrigerator (Oxford Instruments Triton-500). A sensing dot based on an RF single-electron transistor was used to detect the change in the charge state of QD_L, QD_M, and QD_R in our system. An onboard inductor of 1500 nH and a parasitic capacitance on the order of 1 pF formed an LC-tank circuit with a resonance frequency at ~125 MHz, which was used for RF reflectometry. Two arbitrary waveform generators (HDAWG and Operator-X+ by Zurich Instruments and Quantum Machines, respectively) were used to synchronize the multi-channel voltage pulses and timing marker generation. A high-frequency lock-in amplifier (Zurich Instruments, UHFLI) was used as a carrier generator and demodulator for homodyne detection. At room temperature, a carrier power of –40 dBm was generated which was further attenuated by –50 dB by the cryogenic attenuators and the directional coupler. The reflected signal is initially amplified by 50 dB with the cryogenic amplifier (Caltech Microwave Research Group, CITLF2 x2 in series), and then additionally amplified by 20 dB at room temperature using a custom-built RF amplifier. We used the QUA (Quantum Machines) language framework for scripting experimental sequences, performing single-shot readouts, and signal conditioning.

Data availability

The data that support the findings of this study are available from the corresponding author upon request.

Received: 7 November 2023; Accepted: 30 July 2024;
Published online: 14 August 2024

References

1. Loss, D. & DiVincenzo, D. P. Quantum computation with quantum dots. *Phys. Rev. A* **57**, 120–126 (1998).
2. Petta, J. R. et al. Coherent manipulation of coupled electron spins in semiconductor quantum dots. *Science* **309**, 2180–2184 (2005).
3. Koppens, F. H. L. et al. Driven coherent oscillations of a single electron spin in a quantum dot. *Nature* **442**, 766–771 (2006).
4. Nadj-Perge, S., Frolov, S. M., Bakkers, E. P. A. M. & Kouwenhoven, L. P. Spin–orbit qubit in a semiconductor nanowire. *Nature* **468**, 1084–1087 (2010).
5. Van Den Berg, J. W. G. et al. Fast spin-orbit qubit in an indium antimonide nanowire. *Phys. Rev. Lett.* **110**, 066806 (2013).
6. Pioro-Ladrière, M. et al. Electrically driven single-electron spin resonance in a slanting Zeeman field. *Nat. Phys.* **4**, 776–779 (2008).
7. Takeda, K. et al. A fault-tolerant addressable spin qubit in a natural silicon quantum dot. *Sci. Adv.* **2**, e1600694 (2016).
8. Scappucci, G. et al. The germanium quantum information route. *Nat. Rev. Mater.* **6**, 926–943 (2020).
9. Maurand, R. et al. A CMOS silicon spin qubit. *Nat. Commun.* **7**, 13575 (2016).
10. Jock, R. M. et al. A silicon metal-oxide-semiconductor electron spin-orbit qubit. *Nat. Commun.* **9**, 1768 (2018).
11. Maune, B. M. et al. Coherent singlet-triplet oscillations in a silicon-based double quantum dot. *Nature* **481**, 344–347 (2012).
12. Kawakami, E. et al. Electrical control of a long-lived spin qubit in a Si/SiGe quantum dot. *Nat. Nanotechnol.* **9**, 666–670 (2014).
13. Yoneda, J. et al. A quantum-dot spin qubit with coherence limited by charge noise and fidelity higher than 99.9%. *Nat. Nanotechnol.* **13**, 102–106 (2018).
14. Wu, X. et al. Two-axis control of a singlet–triplet qubit with an integrated micromagnet. *Proc. Natl. Acad. Sci.* **111**, 11938–11942 (2014).
15. Takeda, K., Noiri, A., Yoneda, J., Nakajima, T. & Tarucha, S. Resonantly driven singlet-triplet spin qubit in silicon. *Phys. Rev. Lett.* **124**, 117701 (2020).
16. Jock, R. M. et al. A silicon singlet–triplet qubit driven by spin-valley coupling. *Nat. Commun.* **13**, 641 (2022).
17. Cai, X., Connors, E. J., Edge, L. F. & Nichol, J. M. Coherent spin–valley oscillations in silicon. *Nat. Phys.* **19**, 386–393 (2023).
18. Dumoulin Stuyck, N. I. et al. Low dephasing and robust micromagnet designs for silicon spin qubits. *Appl. Phys. Lett.* **119**, 094001 (2021).
19. Reilly, D. J., Marcus, C. M., Hanson, M. P. & Gossard, A. C. Fast single-charge sensing with a rf quantum point contact. *Appl. Phys. Lett.* **91**, 162101 (2007).
20. Noiri, A. et al. Radio-frequency-detected fast charge sensing in undoped silicon quantum dots. *Nano Lett.* **20**, 947–952 (2020).
21. Ono, K., Austing, D. G., Tokura, Y. & Tarucha, S. Current rectification by pauli exclusion in a weakly coupled double quantum dot system. *Science* **297**, 1313–1317 (2002).
22. Orona, L. A. et al. Readout of singlet-triplet qubits at large magnetic field gradients. *Phys. Rev. B* **98**, 125404 (2018).
23. Harvey-Collard, P. et al. High-fidelity single-shot readout for a spin qubit via an enhanced latching mechanism. *Phys. Rev. X* **8**, 021046 (2018).
24. Nakajima, T. et al. Robust single-shot spin measurement with 99.5% fidelity in a quantum dot array. *Phys. Rev. Lett.* **119**, 017701 (2017).
25. Fogarty, M. A. et al. Integrated silicon qubit platform with single-spin addressability, exchange control and single-shot singlet-triplet readout. *Nat. Commun.* **9**, 4370 (2018).
26. Delbecq, M. R. et al. Quantum dephasing in a gated GaAs triple quantum dot due to nonergodic noise. *Phys. Rev. Lett.* **116**, 046802 (2016).
27. Connors, E. J., Nelson, J., Qiao, H., Edge, L. F. & Nichol, J. M. Low-frequency charge noise in Si/SiGe quantum dots. *Phys. Rev. B* **100**, 165305 (2019).
28. Struck, T. et al. Low-frequency spin qubit energy splitting noise in highly purified 28Si/SiGe. *Npj Quantum Inf.* **6**, 40 (2020).
29. Shi, Z. et al. Tunable singlet-triplet splitting in a few-electron Si/SiGe quantum dot. *Appl. Phys. Lett.* **99**, 233108 (2011).
30. Breuer, H.-P. & Petruccione, F. *The Theory of Open Quantum Systems*. (Clarendon, Oxford, 2007).
31. Donahue, M. J. & Porter, D. G. OOMMF User's Guide, Version 1.0. National Institute of Standards and Technology, Gaithersburg, MD (1999).
32. Neumann, R. & Schreiber, L. R. Simulation of micro-magnet stray-field dynamics for spin qubit manipulation. *J. Appl. Phys.* **117**, 193903 (2015).
33. Connors, E. J., Nelson, J., Edge, L. F. & Nichol, J. M. Charge-noise spectroscopy of Si/SiGe quantum dots via dynamically-decoupled exchange oscillations. *Nat. Commun.* **13**, 940 (2022).
34. Zhao, R. et al. Single-spin qubits in isotopically enriched silicon at low magnetic field. *Nat. Commun.* **10**, 5500 (2019).

35. Abe, E. et al. Electron spin coherence of phosphorus donors in silicon: effect of environmental nuclei. *Phys. Rev. B* **82**, 121201 (2010).
36. Deng, C. & Hu, X. Nuclear spin diffusion in quantum dots: effects of inhomogeneous hyperfine interaction. *Phys. Rev. B* **72**, 165333 (2005).
37. Sergeevich, A., Chandran, A., Combes, J., Bartlett, S. D. & Wiseman, H. M. Characterization of a qubit Hamiltonian using adaptive measurements in a fixed basis. *Phys. Rev. A* **84**, 052315 (2011).
38. Shulman, M. D. et al. Suppressing qubit dephasing using real-time Hamiltonian estimation. *Nat. Commun.* **5**, 5156 (2014).
39. Nagaraja, H. S. et al. Magnetic domain studies of cobalt nanostructures. *J. Supercond. Nov. Magn.* **25**, 1901–1906 (2012).
40. Mi, X., Cady, J. V., Zajac, D. M., Deelman, P. W. & Petta, J. R. Strong coupling of a single electron in silicon to a microwave photon. *Science* **355**, 156–158 (2017).
41. Mi, X. et al. A coherent spin–photon interface in silicon. *Nature* **555**, 599–603 (2018).
42. Veldhorst, M. et al. An addressable quantum dot qubit with fault-tolerant control-fidelity. *Nat. Nanotechnol.* **9**, 981–985 (2014).

Acknowledgements
This work was supported by a National Research Foundation of Korea (NRF) grant funded by the Korean Government (MSIT) (No. 2019M3E4A1080144, No. 2019M3E4A1080145, No. 2019R1A5A1027055, RS-2023-00283291, SRC Center for Quantum Coherence in Condensed Matter RS-2023-00207732, No. 2023R1A2C2005809, and RS-2024-00413957) and the core center program grant funded by the Ministry of Education (No. 2021R1A6C101B418). The work on the ^{28}Si/SiGe growth was supported by JST Moonshot R&D grant No. JPMJMS226B and JSPS Grant-in-Aid for Scientific Research (KAKENHI) grant No. JP21H01808. The authors thank Susan Coppersmith for fruitful discussions. Correspondence and requests for materials should be addressed to D.K. (dohunkim@snu.ac.kr).

Author contributions
D.K. conceived and supervised the project. Y.S. and J.K. fabricated the device. Y.S., J.Y., and H.J. performed the measurements and analyzed the data with W.J. J.P., M.C., and H.S. built the experimental setup and configured the measurement software. S.M., N.U., and K.M.I. synthesized and provided the ^{28}Si/SiGe heterostructure. All the authors contributed to the preparation of the manuscript.

Competing interests
The authors declare no competing interests.

Additional information
Supplementary information The online version contains supplementary material available at https://doi.org/10.1038/s41534-024-00869-y.

Correspondence and requests for materials should be addressed to Dohun Kim.

Reprints and permissions information is available at http://www.nature.com/reprints

Publisher's note Springer Nature remains neutral with regard to jurisdictional claims in published maps and institutional affiliations.